### **Review Article**

Fabiola Pineda\*, Carola Martínez, Pablo Martin, and Claudio Aguilar

# High-entropy alloys: A review of their performance as promising materials for hydrogen and molten salt storage

https://doi.org/10.1515/rams-2023-0150 received September 07, 2022; accepted November 06, 2023

Abstract: Fossil fuels have been the most employed energy source with a consistent and growing consumption; however, they will be replaced by renewable energy sources (RESs). Massively using this type of energy will require new materials, especially metallic-based materials, because the typical materials have shown poor performance. In particular, hydrogen obtained from RESs has technological concerns like absorption/desorption cycling, kinetics, and cost. Similarly, the solar industry demands highly corrosionresistant materials at high temperatures. As mentioned above, these could be solved using high-entropy alloys (HEAs). HEAs are barely around 15 years old and have been intensively investigated to be used for wide technological and scientific applications due to their unusual mechanical, physical, and chemical properties. Thus, this study summarizes advances in HEAs as promising materials for hydrogen and energy molten salt storage technologies and discusses the corrosion performance of current HEAs, considering both the microstructure and constituent element effect.

Keywords: high-entropy alloys, hydrogen storage, molten salt

### 1 Introduction

Fossil fuels have been the most widely used energy source. Their consumption continues to grow, which will exhaust

\* Corresponding author: Fabiola Pineda, Centro de Nanotecnología Aplicada, Facultad de Ciencias, Ingeniería y Tecnología, Universidad Mayor, Santiago, 8580745, Chile, e-mail: fabiola.pineda@umayor.cl Carola Martínez: Departamento de Ingeniería en Obras Civiles, Universidad de La Frontera, Francisco Salazar 1145, Temuco, Chile Pablo Martin: Departamento de Ciencia e Ingeniería de Materiales, Universitat Politècnica de Catalunya – BarcelonaTech, 08019, Barcelona, Spain

**Claudio Aguilar:** Departamento de Ingeniería Metalúrgica y de Materiales, Universidad Técnica Federico Santa María, Av. España 1680, Valparaíso, Chile them in the coming years [1]. In addition to climate change, this has impulse the search and implementation of alternative energy resources [2]. Renewable energy sources (RESs) are emerging as one of the most promising alternatives to replacing fossil fuels. They correspond to wind, solar, geothermal, biomass, biogas, wave, tides, and any other electricity generation sources suitable for establishing hydroelectric generation facilities with a channel-or river-type or reservoir area of less than 15 km² [3]. In most cases, the energy is stored for carrier or later use. Hydrogen is one of the most efficient energy carriers, delivering and storing high amounts of energy [4].

Hydrogen storage is done mainly using hydrides based on light elements. However, their high cost and possible degradation after several absorption/desorption cycles have motivated their replacement with novel materials. Among them, high-entropy alloys (HEAs) seem to be a promising option since these have been reported to be better in hydride formation [5]. Similarly, the energy storage from sunlight through concentrated solar power (CSP) technology requires alternative materials because the currently employed materials have a high risk of corrosion. Thus, several authors propose using HEAs for this and other corrosive applications [6–9]. With this motivation, this work aims to review HEAs' qualitative and quantitative performance with the potential to be used as a storage material for hydrogen and solar energy (through molten salts). The data on their microstructure, hydrogen storage capacity, and corrosion performance are discussed. HEAs will be listed alphabetically for ease of reading and their constituent elements. Additionally, their composition will be expressed in molar ratio or atomic percentage (at%).

### 1.1 Hydrogen storage

One of the main objectives of "hydrogen economy" is that it is produced through RES; therefore, hydrogen is emerging as an ideal candidate to carry energy in mobile applications [10].

Moreover, hydrogen presents two significant advantages over other carriers. First, it has a three times higher calorific value than gasoline – 120 MJ·kg<sup>-1</sup> for hydrogen versus 44 MJ·kg<sup>-1</sup> for gasoline [4] – and second, it reduces the adverse environmental outcomes.

As an energy carrier, hydrogen requires a storage medium to be transported from the generation facility to the consumer and the charge-discharge supply centers. However, its low density – 8 MI·L<sup>-1</sup> for liquid hydrogen vs 32 MJ·L<sup>-1</sup> for gasoline – raises concerns regarding storage and transportation [4]. Different storage methodologies have been proposed to reduce this issue, such as compressed gas, a cryogenic liquid, and solid-state storage, either chemically absorbed or physisorbed, like metal hydrides, complex hydrides, and carbon materials [11]. The latter is one of the best options because hydrogen's electronegativity allows the formation of chemical bonds with various elements to form hydrides [12]. The hydrides based on light elements such as Li, Be, B, C, N, O, Na, Mg, Al, Si, and P have been recommended based on hydrogen storage's gravimetric requirements. However, Be, Si, and P can generate toxic hydrides, and therefore, they are discarded. However, Li, Na, C, Mg, and Al form stable hydrides at room temperature (RT), allowing sufficient hydrogen content (>7 wt% H) [13]. Currently, the primary alloying materials for metals hydrides are intermetallic compounds such as AB<sub>5</sub> (1.5 wt% H), AB<sub>2</sub> (2.0 wt% H), AB (1.8 wt% H), A<sub>2</sub>B (3.0 wt% H), V-based alloys (body-centered cubic [bcc], 2.4 wt% H), and Mg-based alloys (2–5% wt% H) [14].  $A_xB_y$  is a class of compounds composed of x atoms of element A and y atoms of element B. These compounds are characterized by a crystal structure in which A atoms occupy the center of icosahedral cages formed by B atoms [15]. To date, most hydrogen storage alloys can effectively store around 2-3 wt% H, but still have problems of slow hydrogen sorption kinetics, an activation process before hydriding (corresponds to the first hydriding cycle [16], degradation, surface passivation, and high cost [17,18]). Hence, other materials are being investigated to generate new hydrides with superior performance [19,20]. HEAs are attractive as potential hydrogen storage since they can form bcc-type structures with high hydrogen storage capacity and significant lattice distortion, making them suitable for forming better hydrides [5].

### 1.2 Molten salt storage

Solar energy appears as one of the most promising RESs supplying in just 1 h the total energy consumed by the planet in 1 year [21]. Solar energy can be transformed

into electricity even on cloudy days by CSP [22], as sunlight is stored in a thermal energy carrier (usually a molten salt mixture at high temperatures) [21,23]. The first and second generations of CSP have used molten nitrate salts, which determine the operational temperatures around 550°C; however, it is expected that the third generation will use carbonate or chloride molten salts as the efficiency of the process must be increased by using supercritical carbon dioxide instead of steam for the Brayton cycle gas turbines; this change requires an operating temperature over 700°C [22]. However, carbonates have a high melting and decomposition temperature, which is detrimental as these mixtures solidify at high temperatures. Besides, as the temperature increases, the metallic elements responsible for storing the mixtures will be significantly more susceptible to corrosion [24]. Similarly, chlorides have the same disadvantages, which make them incompatible with the construction materials of pipes and storage tanks in CSP plants [25]. Therefore, carbonate and chloride molten salts are still being evaluated for massive application in CSP plants and thus nitrate-based molten salt or other mixtures such as sulfates or mixtures based on them could be implemented [23,26-28].

The choice materials for storage of molten salt are Nibased alloys for operational temperatures above 550°C (temperature of the reactor that focuses sunlight), stainless steel between 300 and 550°C (temperature of the hot storage tank), and carbon steel for temperatures below 300°C (temperature of the cold storage tank) [22]. These materials are still being used as they meet one of the main requirements, i.e., the cost. However, they do not meet the technical requirement, as corrosion rates have been reported to be  $94.56-4.04 \times 10^4$  mpy (milli-inch per year) for Nibased alloys,  $3.55-5.22 \times 10^1$  mpy for stainless steel, and  $31.52-2.92 \times 10^5$  mpy for carbon steel. These values imply a limitation in service life for which the recommended corrosion rate for a long-term service should lie between 0.02 and 0.50 mpy [22,26,29-46]. Therefore, alloys such as alumina-forming alloys, super-corrosion resistance alloys, and HEAs have been proposed as potential and competitive alternatives [7,35,47–53]. HEAs have more potential since the mechanical and corrosion performance are superior [52,53].

#### 1.3 HEAs

HEAs correspond to a promising class of metallic materials independently proposed by Cantor *et al.* [54] and Yeh *et al.* [55] in 2004. These alloys were defined as those constituted by five or more chemical elements, each between 5 and 35 at%, aiming to obtain simple solid solutions boosted by

the high ideal configurational entropy. Notwithstanding, the formation of multi-phase (MP) microstructures (that may include a mixture of solid solutions but also the presence of intermetallic compounds) is typically observed in these alloys and is even more frequent than in single-phase solid solution microstructures [56-58]. HEAs can be classified into subfamilies according to the nature of the components. The most studied subfamily corresponds to the 3d transition metal HEAs (3d TM HEAs), constituted by at least four of the following elements: Fe, Ni, Co, Al, Mn, Cr, Cu, Ti, and V [6], that typically crystallizes into face-centered cubic (fcc) solid solutions. The second most crucial subfamily of HEAs is the refractory high-entropy alloys (RHEA), proposed in 2010 by Senkov et al. [59]. These alloys are constituted mainly by elements from the group's IV, V y VIB – Ti, Zr, Hf, V, Nb, Ta, Cr, Mo, and W – typically exhibiting a disordered bcc solid solution. The most significant aspect of RHEAs is their outstanding mechanical strength at high temperatures, even superior to the traditional Ni-based superalloys [60]. A most recently developed HEA group is based on hexagonal close packing (hcp) solid solutions, constituted by lightweight elements, like Ti, Mg, Li, Y, and Sc, among others [61-63], resulting in lightweight HEAs with interesting properties. Figure 1 shows the possible crystalline structures of HEA used in energy storage.

# 2 HEAs with the potential to be used in storage systems of RES systems

### 2.1 Hydrogen storage

Table 1 summarizes the main HEAs studied regarding hydrogen storage performance. Most of these alloys exhibit

single-phase C14 Laves or bcc solid solution microstructures. Laves phases correspond to a subfamily of intermetallic phases (that groups C14, C15, and C36 Laves phases), typically observed in Cr-, Ti-, and Nb-containing 3d TM HEAs. According to Yurchenko *et al.* [64], these phases are formed when high Allen's electronegativity difference ( $\Delta\chi$ Allen) and high lattice distortion ( $\delta$ ) values are achieved ( $\Delta\chi$ Allen > 7% and  $\delta$  > 5%, respectively). On the other hand, bcc solid solutions are formed with low  $\delta$  and close to zero enthalpies of mixing  $\Delta H^{\rm m}$  values; however, this lattice structure is preferred to sustain higher  $\delta$  values than fcc structures [65]. Because a high  $\delta$  value provides more significant interstitial sites to accommodate hydrogen atoms [5], bcc- and Laves phase-based HEAs are promising candidates for hydrogen storage applications.

In the context of single-phase HEAs, the first approach related to hydrogen storage was made by Kao et al. [66] in 2010. The authors studied the influence of Ti, V, and Zr contents in the CoFeMnTi<sub>x</sub>V<sub>y</sub>Zr<sub>z</sub> alloy (0.5  $\leq$  x  $\leq$  2.5, 0.4  $\leq$  $y \le 3.0$ , and  $0.4 \le z \le 3.0$ ) on the hydrogen absorption–desorption performance using the mass flow pressure concentration isotherm method (PCT test [67]). All the alloys showed a C14 Laves structure, which has been reported with promising stability performance for hydrogen absorption kinetics and maximum hydrogen capacity. The results indicated that the interstitial sites' size influenced the hydrogen adsorption capacity and the pressure plateau during the PCT test, reaching the highest hydrogen absorption in the CoFeMnTi<sub>2</sub>VZr and CoFeMnTiVZr<sub>2.3</sub> alloys – 1.80 and 1.79 wt%, respectively. This may be attributed to the higher atomic radius of Ti and Zr (1.47 and 1.60 Å, respectively) compared to the rest of the constituent elements, which enlarges the interstitial sites of the alloys and thus expands the lattice. Therefore, Ti and Zr are more effective than V in improving hydrogen-to-metal ratio (H/M)<sub>max</sub> for a given molar ratio. Chen et al. [68] reported the influence of the elements in the C14-Cr<sub>u</sub>Fe<sub>v</sub>Mn<sub>w</sub>Ti<sub>x</sub>V<sub>v</sub>Zr<sub>z</sub> alloy. The

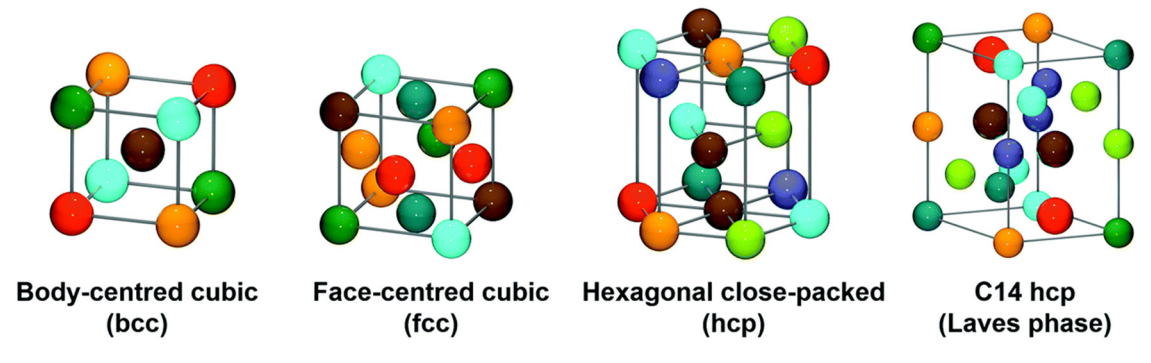


Figure 1: Crystalline structures of HEAs employed in energy-related fields [115].

**Table 1:** Summary of the microstructures, lattice parameters, and the maximum hydrogen storage

Alloy	Microstructures before hydriding	Lattice parameters	Hydrogen storage			
		before hydriding [nm]	Hydrogen absorption [wt%]	Desorption temperature [°C]	Ref	
AlCrFeMnNiW (molar ratio)	bcc + fcc	a = 0.3152 (fcc) a = 0.3860 (bcc)	0.61	300	[83]	
CoFeMnTiVZr (molar ratio)	C14 Laves phase	a = 0.4972 c = 0.8105	1.7	_	[70]	
CoFeMnTiVZr <sub>0.4</sub> (molar ratio)	C14 Laves phase	a = 4.866 c = 7.915	0.03	_	[66]	
CoFeMnTiVZr <sub>0.7</sub> (molar ratio)		a = 4.866 c = 7.936	0.49		[66]	
CoFeMnTiVZr (molar ratio)		a = 4.958 c = 8.046	1.43		[66]	
CoFeMnTiVZr <sub>1.3</sub> (molar ratio)		a = 4.994 c = 8.169	1.63		[66]	
CoFeMnTiVZr <sub>1.6</sub> (molar ratio)		a = 5.031 c = 8.222	1.71		[66]	
CoFeMnTiVZr <sub>2</sub> (molar ratio)		a = 5.056 c = 8.258	1.73		[66]	
CoFeMnTiVZr <sub>2.3</sub> (molar ratio)		a = 5.067 c = 8.302	1.79		[66]	
CoFeMnTiVZr <sub>2.6</sub> (molar ratio)		a = 5.117 c = 8.319	1.73		[66]	
CoFeMnTiVZr <sub>3</sub> (molar ratio)		a = 5.117 c = 8.763	1.56		[66]	
CoFeMnTiV <sub>0.4</sub> Zr (molar ratio)		a = 4.958 c = 8.095	1.48	_	[66]	
CoFeMnTiV <sub>0.7</sub> Zr (molar ratio)		a = 4.970 c = 8.113	1.52		[66]	
CoFeMnTiVZr (molar ratio)		a = 4.958 c = 8.046	1.43		[66]	
CoFeMnTiV <sub>1.3</sub> Zr (molar ratio)		a = 4.958 c = 8.095	1.55		[66]	
CoFeMnTiV <sub>1.6</sub> Zr (molar ratio)		a = 4.970 c = 8.135	1.54		[66]	
CoFeMnTiV <sub>2</sub> Zr (molar ratio)		a = 4.958 c = 8.095	1.55		[66]	
CoFeMnTiV <sub>2.3</sub> Zr (molar ratio)		a = 4.958 c = 8.095	1.58		[66]	
CoFeMnTiV <sub>2.6</sub> Zr (molar ratio)		a = 4.970 c = 8.135	1.64		[66]	
CoFeMnTiV₃Zr (molar ratio)		a = 4.970 c = 8.113	1.62		[66]	
CoFeMnTi <sub>0.5</sub> VZr (molar ratio)		a = 4.960 c = 8.030	0.6	_	[66]	
CoFeMnTiVZr (molar ratio)		a = 4.958 c = 8.046	1.43		[66]	
CoFeMnTi <sub>1.5</sub> VZr (molar ratio)		a = 4.983 c = 8.106	1.78		[66]	
CoFeMnTi <sub>2</sub> VZr (molar ratio)		a = 5.006 $c = 8.155$	1.8		[66]	
CoFeMnTi <sub>2.5</sub> VZr (molar ratio)		a = 5.083 c = 8.220	1.2		[66]	
Co <sub>0.5</sub> Fe <sub>0.5</sub> MgNi <sub>0.5</sub> TiZr (molar ratio) Co <sub>0.5</sub> Fe <sub>0.5</sub> MgNi <sub>0.5</sub> TiZr (molar ratio)	bcc fcc	a = 0.3075(6) a = 0.4642(6)	1.2 0.36	— 375	[79] [79]	
CrFeMgTiV (molar ratio)		a = 0.295	0.3	360	[85]	

Table 1: Continued

Alloy	Microstructures before	Lattice parameters	Hydrogen storage		
	hydriding	before hydriding [nm]	Hydrogen absorption [wt%]	Desorption temperature [°C]	Ref
CrFeMnNiTiZr (molar ratio)	C14 Laves phase + cubic	a = 0.493 c = 0.809	1.7	_	[71]
FeMnTiVZr (molar ratio)	C14 Laves phase	a = 5.020 c = 8.211	1.88	358	[68]
Cr <sub>0.5</sub> FeMnTiVZr (molar ratio)	C14 Laves phase	a = 4.995 c = 8.167	1.71	372	[68]
Cr <sub>0.75</sub> FeMnTiVZr (molar ratio)	C14 Laves phase	a = 4.987 c = 8.162	1.6	405	[68]
CrFeMnTiVZr (molar ratio)	C14 Laves phase	a = 4.982 c = 8.132	1.5	379	[68]
Cr <sub>1.25</sub> FeMnTiVZr (molar ratio)	C14 Laves phase	a = 4.977 $c = 8.128$	1.47	_	[68]
Cr <sub>1.5</sub> FeMnTiVZr (molar ratio)	C14 Laves phase	a = 4.974 c = 8.113	1.47	_	[68]
Cr <sub>2</sub> FeMnTiVZr (molar ratio)	C14 Laves phase	a = 4.969 c = 8.083	1.23	_	[68]
CrMnTiVZr (molar ratio)	C14 Laves phase + hcp	a = 5.056 c = 8.195	1.92	395	[68]
CrFe <sub>0.5</sub> MnTiVZr (molar ratio)	C14 Laves phase	a = 5.028 c = 8.193	1.93	385	[68]
CrFeMnTiVZr (molar ratio)	C14 Laves phase + bcc	a = 4.920 c = 8.090	1.72	370	[68]
CrFe <sub>1.5</sub> MnTiVZr (molar ratio)	C14 Laves phase + bcc	a = 4.915 c = 8.069	1.43	_	[68]
CrFe <sub>2</sub> MnTiVZr (molar ratio)	C14 Laves phase + bcc	a = 4.909 c = 8.068	1.18	_	[68]
CrFeTiVZr (molar ratio)	C14 Laves phase	a = 5.033 c = 8.233	1.78	305	[68]
CrFeMn <sub>0.5</sub> TiVZr (molar ratio)	C14 Laves phase	a = 5.009 c = 8.204	1.71	369	[68]
CrFeMn <sub>0.75</sub> TiVZr (molar ratio)	C14 Laves phase	a = 4.985 c = 8.147	1.61	389	[68]
CrFeMn <sub>1.25</sub> TiVZr (molar ratio)	C14 Laves phase	a = 4.964 c = 8.160	1.47	_	[68]
CrFeMn <sub>1.5</sub> TiVZr (molar ratio)	C14 Laves phase	a = 4.959 c = 8.143	1.27	_	[68]
CrFeMn <sub>2</sub> TiVZr (molar ratio)	C14 Laves phase	a = 4.948 c = 8.136	1.2	_	[68]
CrFeMnVZr (molar ratio)	C14 Laves phase + bcc	a = 4.990 c = 8.186	1.19	_	[68]
CrFeMnTi <sub>0.5</sub> VZr (molar ratio)	C14 Laves phase + bcc	a = 4.976 c = 8.156	1.25	_	[68]
CrFeMnTi <sub>1.5</sub> VZr (molar ratio)	C14 Laves phase	a = 4.986 c = 8.164	1.7	350	[68]
CrFeMnTi <sub>2</sub> VZr (molar ratio)	C14 Laves phase	a = 5.004 c = 8.177	1.85	_	[68]
CrFeMnTiZr (molar ratio)	C14 Laves phase + hcp	a = 4.956 c = 8.133	1.54	340	[68]
CrFeMnTiV <sub>0.5</sub> Zr (molar ratio)	C14 Laves phase	a = 4.977 c = 8.158	1.74	345	[68]
CrFeMnTiV <sub>1.5</sub> Zr (molar ratio)	C14 Laves phase + bcc	a = 4.974 c = 8.149	1.68	370	[68]

6 — Fabiola Pineda et al. DE GRUYTER

Table 1: Continued

Alloy	Microstructures before	Lattice parameters	Hydrogen storage			
	hydriding	before hydriding [nm]	Hydrogen absorption [wt%]	Desorption temperature [°C]	Ref	
CrFeMnTiV <sub>2</sub> Zr (molar ratio)	C14 Laves phase + bcc	a = 4.993	1.85	350	[68]	
		c = 8.168				
CrFeMnTiVZr <sub>0.5</sub> (molar ratio)	C14 Laves phase + bcc	a = 4.919	0.83	_	[68]	
		c = 8.055				
CrFeMnTiVZr <sub>1.5</sub> (molar ratio)	C14 Laves phase	a = 5.030	1.8	355	[68]	
		c = 8.232				
CrFeMnTiVZr <sub>2</sub> (molar ratio)	C14 Laves phase + hcp	a = 5.071	1.82	345	[68]	
		c = 8.294				
$Cr_{13.5}Fe_{15.8}Ni_{16.0}Ti_{16.2}V_{22.2}Zr_{16.3}$ (at%)	C14 Laves phase + hcp	a = 0.4969  (C14)	1.81	_	[84]	
		c = 0.8126  (C14)				
CrFeNiTiVZr (molar ratio)	C14 Laves phase	a = 0.5017	1.6	_	[69]	
		c = 0.8191				
Cr <sub>0.5</sub> MgMn <sub>0.5</sub> NbNi <sub>0.5</sub> Ti (molar ratio)	bcc	a = 0.32893(9)	1.6	380	[72]	
HfMoScTiZr (molar ratio)	bcc	a = 0.3444	2.14	_	[74]	
HfNbTaTiZr (molar ratio)	bcc	a = 0.3399	1.66	375	[80]	
$Hf_{20}Mo_{20}Nb_{20}Ti_{20}Zr20$ (at%)	bcc	a = 0.3370(2)	1.18	302	[75]	
$Hf_{20}Nb_{40}Ti_{20}Zr20$ (at%)	bcc	a = 0.3423(1)	1.12	383	[76]	
$Hf_{20}Mo10Nb_{30}Ti_{20}Zr_{20}$ (at%)		a = 0.3402(2)	1.54	332	[76]	
$Hf_{20}Mo_{20}Nb_{20}Ti_{20}Zr_{20}$ (at%)		a = 0.3370(1)	1.18	302	[76]	
$Hf_{20}Mo_{30}Nb_{10}Ti_{20}Zr_{20}$ (at%)		a = 0.3357(1)	1.4	164	[76]	
$Hf_{20}Mo_{40}Ti_{20}Zr_{20}$ (at%)		a = 0.3327(1)	0.92	168	[76]	
HfNbTiVZr (molar ratio)	bcc	a = 0.33659(2)	1.8	500	[81]	
		_	2.7	400	[5]	
MoNbTiVZr (molar ratio)	bcc + orthorhombic NbTi4- type phase	<i>a</i> = 0.325	2.3	_	[116]	
NbTaTiZr (molar ratio)	bcc	a = 0.33647	1.67	_	[117]	
NbTaTiZr (molar ratio)	bcc	a = 0.33647	1.6	_	[118]	
Nb <sub>23</sub> Ta <sub>25</sub> Ti <sub>26</sub> V <sub>26</sub> (at%)	bcc	_	1.86	112	[82]	
Nb <sub>20</sub> Ti <sub>27</sub> V <sub>27</sub> Zr <sub>26</sub> (at%)		_	2.83	300	[82]	
Nb <sub>18</sub> Ti <sub>21</sub> V <sub>21</sub> Zr <sub>41</sub> (at%)		_	2.66	390	[82]	
Nb <sub>27.5</sub> Ti <sub>32.5</sub> V <sub>27.5</sub> Zr <sub>12.5</sub> (at%)	bcc	a = 0.3261(1)	2.5	250	[77]	
27.3 32.3 27.3 12.3 (****)		a = 0.3270(1)	2.5	430	[77]	
		a = 0.3277(1)	2	400	[77]	
Nb <sub>2 5</sub> TaTi <sub>3</sub> V <sub>2 5</sub> Zr (molar ratio)	bcc	a = 0.3263(1)	2.5	262	[78]	

<sup>-:</sup> Non reported; am: amorphous phase.

results show that Ti and Zr are H-absorbing A elements, while the other four are H-desorbing B elements in  $AB_2$ . Ti and Zr increase the maximum hydrogen absorption, while Cr, Fe, and Mn decrease the hydrogen absorption. Although V is the B element in  $AB_2$ , the amount of V in the alloy has no significant effect on hydrogen absorption.

In contrast, the kinetic parameter can be defined by employing the  $t_{90}$  indicator, which is the time necessary for the alloy or system to absorb 90% of the total hydrogen absorption capacity. The kinetic parameter increases with increasing  $Cr_{uv}$   $Fe_{vv}$ , and  $Mn_{uv}$  but decreases with increasing  $Zr_{zv}$ , while there is no regular trend with  $Ti_x$  and  $V_y$ . The

lowering of the kinetic parameter with  $Zr_z$  is ascribed to the atomic size of Zr, which is the largest among different atoms, giving the easiest way for H diffusion.

Zadorozhnyy *et al.* [69] and Sarac *et al.* [70] reported single-phase CrFeNiTiVZr and CoFeMnTiVZr HEAs, both alloys exhibiting C14 Laves phase. These authors compared the absorption capacity by either solid–gas reaction or electrochemical methods in an Ar-saturated 6 M KOH solution. CrFeNiTiVZr reached 1.6 wt% by both methodologies, while the CoFeMnTiVZr alloy reached 1.7 and 1.9 wt% by solid–gas reaction and electrochemical testing, respectively. Based on these results, the electrochemical method seems

appropriate to describe the hydrogen sorption/desorption kinetics and their hydrogen storage capacity for the materials with shallow hydrogen storage capacity, which might not be possible to detect using the gas—solid reactions method. A similar microstructure was observed in the CrFeMnNiTiZr alloy [71], reaching 1.6 wt% of hydrogen absorption during the first hydriding cycle without any activation process, and 1.7 wt% in the third cycle. Moreover, hydrogen desorption occurred almost without hysteresis in the PCT isotherms.

Marques *et al.* [72] analyzed the hydrogen storage behavior of MgTiNbCr<sub>0.5</sub>Mn<sub>0.5</sub>Ni<sub>0.5</sub> obtained by reactive milling. The two phases obtained correspond to the bcc and fcc structures. By thermal analysis, two endothermic peaks were determined to be attributed to the desorption process of Mg<sub>2</sub>NiH<sub>4</sub>, which occurs at approximately 250°C, and the second peak is associated with the desorption of the fcc hydride, which occurs at about 380°C. The formation of Mg<sub>2</sub>NiH<sub>4</sub> is because the Mg exhibited a high positive  $\Delta H^{\rm mix}$  (indicating immiscibility) with most elements except Mg–Ni, which has  $\Delta H^{\rm mix}$  (4 kJ·mol<sup>-1</sup>), indicating a tendency to form intermediate phases as Mg<sub>2</sub>Ni, which is the precursor of Mg<sub>2</sub>NiH<sub>4</sub> [73].

In contrast, Hu et al. [74] determined the structural and electronic properties of hydriding HfMoScTiZr under different hydrogen concentrations using the density functional theory method. The results showed that the bcc HfMoScTiZr alloy reached a maximum of 2.14 wt%, attributable to an increase in the lattice parameter due to the addition of hydrogen. Additionally, the results indicate that hydrogen was located in both tetrahedral and octahedral interstitial sites. Shen et al. [75,76] studied the Hf<sub>20</sub>Mo<sub>x</sub>Nb<sub>y</sub>.  $Ti_{20}Zr_{20}$  (with x + y = 40 at%, and x = 0, 10, 20, 30, and 40 at%) HEAs, analyzing the Mo effect on their hydriding performance. The authors reported that the hydride-forming capacity decreases as the Mo content increases, while a bcc SPSS microstructure is observed in all the alloys. The maximum hydrogen storage capacity (1.54 wt%) was obtained with x = 10% in the sample, indicating that increasing the Mo concentration decreased the cell volume. Likewise, the desorption temperature decreases with increasing Mo content, reaching the lowest value at 30 at% Mo (164°C). This indicates that the thermal stability can be correlated to the increasing weakness of the bond between hydrogen and the Hf<sub>20</sub>Mo<sub>x</sub>Nb<sub>ν</sub>Ti<sub>20</sub>Zr<sub>20</sub> alloys as the Mo content increased. Montero et al. [77,78] reported that the bcc SPSS NbTaTiVZr alloy forms a hydride compound with fcc ( $Fm\bar{3}m$  space group) or body-centered tetragonal (bct) lattice structure (I4/mmm space group) after the hydrogen absorption process. The bct lattice can be interpreted as a slightly distorted fcc lattice. This transformation (bcc  $\rightarrow$  fcc (or bct)) has also been reported in other HEAs [5,75–77,79–81]. In particular, the NbTaTiVZr alloy reached its maximum absorption (2.5 wt%) in just 2 min at 100°C, presenting a fast absorption rate in a single step [78]. Nygård  $et\ al.$  [82] studied the effect of Zr in the bcc NbTiVZr HEAs and found that as the amount of Zr increased, the stability of the hydride formed also increased. This may result in a disadvantage since the total desorption of the Nb<sub>18</sub>Ti<sub>21</sub>V<sub>21</sub>Zr<sub>41</sub> (at%) alloy was reached at 900°C.

Dewangan et al. [83] reported a microstructure composed of fcc + bcc phases in the AlCrFeMnNiW alloy regarding MP HEAs. The hydrogen sorption was measured through the volumetric method at RT and atmospheric pressure, resulting in a maximum storage capacity of 0.616 wt% after a single exposure and a desorption activation energy of  $-8.16 \text{ kJ} \cdot \text{mol}^{-1}$ . Kunce et al. [84] reported C14 Laves phase + hcp in the CrFeNiTiVZr alloy. After the hydrogen desorption, the C14 hydride phase was observed too. The heat-treated sample - subjected to heating at 1,000°C for 24 h - has a lower hydrogen absorption capacity than the untreated sample (1.56 and 1.81 wt%, respectively). This difference may be associated with a more relaxed crystal lattice due to a more homogeneous composition resulting from the heat treatment. de Marco et al. [85] reported the CrFeMgTiV alloy with a bcc + amorphous phase microstructure. The results showed that the alloy could only absorb hydrogen at 350°C with a hydrogen storage capacity of 0.3 wt%. Additionally, there was no evidence of a defined pressure plateau associated with amorphous phases, hindering hydrogen atom reorganization.

HEAs have high hydrogen solubility and can quickly form hydrides, making them promising for hydrogen storage; however, this can cause mechanical and chemical degradation. The HEAs' nature can also lead to phase transformations, affecting their properties during repeated hydrogen absorption and release. The thermodynamics and kinetics of hydrogen transport in HEAs are complex and need to be better understood [86,87]. The cost and scalability of producing HEAs for hydrogen storage also need further investigation. HEAs show promise for metal storage *via* interstitial hydrogen or hydride formation [5,15], but optimizing their properties and evaluating their long-term durability and reliability is necessary.

### 2.2 Molten salt storage

Table 2 presents the available data related to corrosion studies of HEAs exposed to simulated conditions of CSP

Table 2: Summary of the microstructure and corrosion test data of HEAs exposed to molten salts

Alloy	Microstructure	Corrosion test				
		Technique employed	Exposure conditions [h/°C]	Molten salt	Corrosion rate (original unit)	
Al <sub>2.4</sub> Co <sub>24.3</sub> Cr <sub>24.5</sub> Fe <sub>24.4</sub> Ni <sub>24.4</sub> (at%)	_	Electrochemical	1/750	Na <sub>2</sub> SO <sub>4</sub> -25 wt % NaCl	31 mpy [89]	
$Al_4Co_{22}Cr_{12}Fe_{12}Ni_{44}Ti_6$ (at%)	_	Gravimetric	200/900	Na <sub>2</sub> SO <sub>4</sub> -25 wt	2.9 mg·cm <sup>-2</sup> [90]	
$Al_4Co_{22}Cr_{12}Fe_{12}Ni_{44}Ti_6$ (at%)			200/1100	% NaCl	14.3 mg·cm <sup>-2</sup> [90]	
Al <sub>5</sub> Co <sub>18</sub> Cr <sub>7</sub> Fe <sub>9</sub> Ni <sub>51</sub> Ti <sub>5</sub> (at%)			200/900		1.9 mg·cm <sup>-2</sup> [90]	
$Al_5Co_{18}Cr_7Fe_9Ni_{51}Ti_5$ (at%)			200/1100		2.0 mg·cm <sup>-2</sup> [90]	
CoCrFeMnNi (molar ratio)	fcc	Electrochemical	50/500	Solar salt	- [98]	
CoCrFeNiTi <sub>0.5</sub> (molar ratio)	_	Gravimetric	150/750	$Na_2SO_4$ -25 wt% $K_2SO_4$	1.4 mg·cm <sup>-2</sup> [104]	
				Na <sub>2</sub> SO <sub>4</sub> -25 wt % NaCl	2.27 mg·cm <sup>-2</sup> [104]	
Cr <sub>18</sub> Fe <sub>27.5</sub> Mn <sub>27</sub> Ni <sub>27.5</sub> (at%)	fcc	Gravimetric	1,000/700	FLiBe	-3.4 mg·cm <sup>-2</sup> [102]	

(direct contact with molten salts at high temperatures). These studies were carried out on a laboratory scale because the metallic materials are encapsulated in closed and isolated systems (to avoid thermal losses) [22]; thus, it is challenging to perform these studies in CSP plants. Consequently, the most accurate strategy to test new metallic materials involves examining the laboratory specimens through gravimetric and electrochemical techniques [22]. The gravimetric test is the most straightforward methodology, which compares the initial weight of a coupon with the weight after exposure to the corrosive medium. The difference in weight (loss or gain, depending on the oxide layer's adherence) determines the corrosion rate and its mathematical function. However, this method has significant disadvantages. The most important are (i) the time interval selection may not include changes or critical aspects of the corrosion mechanism and (ii) low reliability in localized corrosion [88]. Conversely, the electrochemical tests, i.e., electrochemical polarization and electrochemical impedance spectroscopy, can provide corrosion rate information and insights into the involved chemical reactions and the corrosion product's properties [22].

Jalbuena *et al.* [89] studied the  $Al_{2.4}Co_{24.3}Cr_{24.5}Fe_{24.4}Ni_{24.4}$  (at%), comparing their performance with a commercial alloy, the Haynes 718 Ni-based alloy. Similarly, Tsao *et al.* [90] studied  $Al_4Co_{22}Cr_{12}Fe_{12}Ni_{44}Ti_6$  and  $Al_5Co_{18}Cr_7Fe_9Ni_{51}Ti_5$  HEAs (at%) to compare their results with the CM247LC Ni-based superalloy. All the alloys were exposed to the same electrolyte; the results showed a higher corrosion resistance for HEA in the first case. The superior performance of  $Al_{2.4}Co_{24.3}Cr_{24.5}Fe_{24.4}Ni_{24.4}$  was attributed to the development of a protective oxide layer – with high thermal stability, good adherence, and continuous and slow growth [91] – of

a duplex structure made of Cr<sub>2</sub>O<sub>3</sub> as the outer layer, and Al<sub>2</sub>O<sub>3</sub> as the inner layer. The outer layer interrupts the corrosive process by interacting with elements from the salt, which generates a positive solubility gradient that retards the process. At the same time, the inner layer extends the initial stage of corrosion and hinders its propagation. The alloys studied by Tsao et al. did not show Cr<sub>2</sub>O<sub>3</sub> and Al<sub>2</sub>O<sub>3</sub> layers in the initial stages of the corrosion process, which was associated with low corrosion resistance. However, the authors point out that the difference in Al content can influence corrosion resistance. Besides, several studies report that an increase in Al content in the Al<sub>x</sub>CoCrFeNi HEA induces the formation of bcc-disordered (A2) and bcc-ordered (B2) phases in the replacement of fcc solid solution [92-95]. Yeh et al. [55] reported that the Al<sub>x</sub>CoCrFeNi HEAs evolved from an fcc SPSS to an MP fcc + A2/B2 alloy when the Al content exceeded x = 0.8.

Moreover, the fcc phase was no longer observed when the Al content was higher than x = 2.8. This phase transformation is strictly related to the lattice strain imposed by the addition of Al [65,96,97]. As Al has a larger atomic size than Cr, Fe, and Ni [57], a significant lattice distortion is expected. Due to the fcc phase having a higher packing factor than the bcc phase, less lattice strain may be stored, destabilizing the fcc phase. Consequently, and as mentioned previously, a bcc phase is preferred when large values of lattice distortion are expected [65].

Moon *et al.* [98] analyzed the CoCrFeMnNi alloy, one of the most widely studied HEAs as it was the first SPSS HEA [99–101]. The results were compared with 4130 steel, 316L stainless steel, and 800 Ni-based alloys. A similar alloy was studied by Elbakhshwan *et al.* [102], who compared the fcc SPSS  $Cr_{18}Mn_{27}Fe_{27.5}Ni_{27.5}$  (at%) with AISI 316H stainless

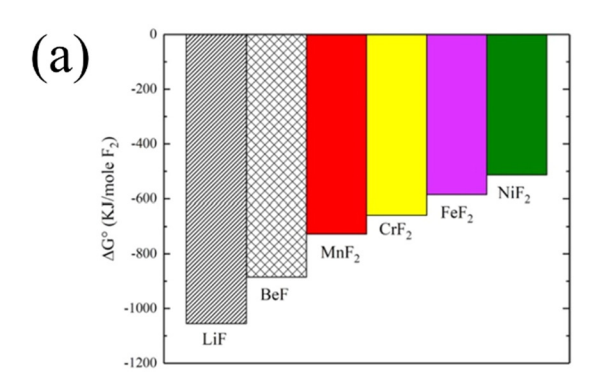
steel. Both HEAs showed higher corrosion than commercial alloys. In the first case, this was associated with developing a non-protective oxide layer mainly consisting of Fe-based spinel. Even though this HEA has Cr and Ni - elements traditionally associated with high corrosion resistance corrosion products could not be developed as they were depleted with surprisingly high leaching rates. Presumably, this is because of the high dissolution driving force of both elements in the molten salt, which alongside its high content, induces further deterioration. This was not the case with Cr<sub>18</sub>Mn<sub>27</sub>Fe<sub>27</sub> <sub>5</sub>Ni<sub>27</sub> <sub>5</sub>, as Cr dissolution was considerably lower. Thus, the lower corrosion resistance was attributed to the more negative Gibbs free energy of the formation of  $MnF_2$  (730 kJ·mol<sup>-1</sup>  $F_2$ ) compared with  $CrF_2$  (650 kJ·mol<sup>-1</sup>  $F_2$ ), as shown in Figure 2a. Note that the Gibbs free energy of formation can also be used to make other types of thermodynamic predictions, such as the one made by Zhao et al., who studied a ternary mixture of molten chloride salts subjected to different purification methods based on thermal and chemical treatments associated with the reduction of magnesium, for its potential use in solar thermal plants. The authors indicated that the control of impurities would be effective when generating cations with more negative Gibbs free energy than Mg cations as the ones on the right-hand side of Figure 2b, since these would be stable and remove impurities in the salt, reducing its corrosivity [103].

**DE GRUYTER** 

Additionally, the higher diffusion coefficient of Mn hinders Cr dissolution. However, Cr was found to be associated with bcc precipitates related to internal corrosion in the HEA. As the depth increased, an increase in precipitate population and a change in their morphology (from spherical to needle-shaped) were observed. These variations were also associated with differences in the Mn concentration through the bulk. Based on this, the authors preliminary concluded that Mn could act as a sacrifice element, or well, as a salt redox buffer through the Mn/MnF<sub>2</sub> couple.

Note that many other commercial and experimental (no HEA alloy) have been studied for CSP use. Our group describes a comprehensive overview of their performance in the study of Walczak et al. [22]. Two carbon and low alloy steel groups can be highlighted in general terms. ASTM A36 and A516 gr 70 are according to the industry guidelines; thus, they are recommended for components of CSP plants. However, these alloys are highly affected by some elements that, in some cases, are impurities of molten salts, particularly chlorides. This is different for stainless steel, from which AISI 347 and AISI 347H are highlighted as they maintain low corrosion rates at the highest operating temperatures of CSP. However, they might become obsolete in the next generation of CSP, in which the operating temperatures will increase. In this context, the recommendation is a superalloy like Hastelloy, Inconel, or Incoloy.

Regarding the electrolyte, Ping et al. [104] studied the CoCrFeNiTi<sub>0.5</sub> HEA by exposing it to Na<sub>2</sub>SO<sub>4</sub>-25% K<sub>2</sub>SO<sub>4</sub> and Na<sub>2</sub>SO<sub>4</sub>-25% NaCl molten salts. As was expected, the presence of Cl in the electrolyte increase corrosion due to this ion catalysing the process through the cyclic chlorination/oxidation mechanism, leading to irregular and porous corrosion products that crack and spall with time. This has also been observed for HEAs in other electrolytes, for example, at 3.5 wt% NaCl solution and artificial seawater, although unrelated to energy storage, are related to renewable energy such as wave, tidal, and ocean thermal [105-107]. Similarly, HEAs have attracted the attention of the geothermal industry as their efficiency can be improved using metal materials with high mechanical strength, high oxidation resistance, and low density [8,9,53,108-114]. However, in all cases, there is a high risk of corrosion; thus, it will be developed as a separate topic in an exclusive study that we hope to publish in the future.



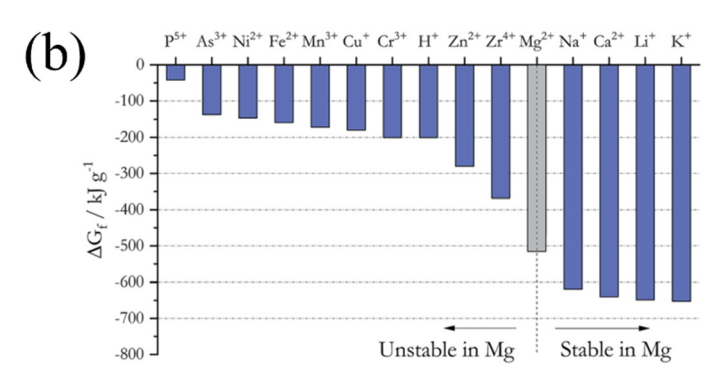


**Figure 2:** (a) Gibbs free energy of formation of different fluoride compounds at 700°C [102] and (b) Gibbs free energy of formation of different chloride compounds at 827°C [103].

# 3 Concluding remarks

The study of RES has provided significant advances in the past years, offering a viable opportunity to mitigate the use of fossil fuels. Consequently, the demand for new materials that satisfy the growing need for ever-greener and cheaper energy has become an issue. In particular, the necessity of new materials to overcome the challenges in hydrogen and molten salt storage has prompted research into HEAs and RHEAs. The latter had stood out for their mechanical behavior in the past. However, their corrosion had yet to be mostly commented on, so it was convenient to study and compare the results reported to date in this work to address further development in the industry.

So far, the HEAs with a single-phase bcc have shown promising results regarding hydrogen storage due to a higher capacity to sustain lattice distortion than fcc- or hcp-based HEAs. The higher hydrogen absorption values are over 2 wt%, for HfNbTiVZr, MoNbTiVZr, and NbTiVZr alloys. Conversely, MP HEAs were reported with low absorption and desorption capacities, such as AlCrFeMnNiW (0.61 wt%), CoFeMnTiVZr<sub>0.4</sub> (0.03 wt%), and CoFeMnTiVZr<sub>0.7</sub> (0.49 wt%). Hence, it is necessary to enhance the design and phase formation prediction of HEAs to establish clear guidelines for the stability of single-phase microstructure with bcc lattice structure. Although extensive advances have been made during the last few years using semi-empirical parameters, CALPHAD, machine learning approaches, and even combined approaches, most have mainly focused on fcc-based and 3d TM HEAs. Also, the study of the effect of the constituent elements requires further clarification since good results were found with the addition of titanium and zirconium to CoFeMn-based alloys but not with molybdenum's addition to the HfMoxNbyTiZr alloy. Future investigations are recommended to develop an HEA that has high cyclability and lower desorption temperature. HEAs are a promising material class for hydrogen storage due to their high surface area, mechanical strength, and high hydrogen solubility. These properties make HEAs well-suited for applications requiring efficient and rapid hydrogen storage and release. HEAs also have excellent mechanical properties that help prevent mechanical failure and degradation during repeated hydrogen absorption/desorption cycles. However, challenges remain in optimizing the composition and microstructure of HEAs for maximum hydrogen storage capacity, and efficiency, and developing cost-effective manufacturing and processing methods. Despite these challenges, the potential advantages of HEAs make them a promising area of research and development in the renewable energy sector. HEAs could play an essential role in the transition to a more sustainable and environmentally friendly energy system by providing a reliable and efficient source of hydrogen storage.

In the context of solar energy, HEAs have been demonstrated to be a competitive alternative to the current choice. HEAs' superior corrosion resistance was achieved with aluminum as one of the constituent elements since it can develop along with chromium. This protective oxide multilayer covers the entire metallic surface hindering further attack from molten salts. Similarly, using sacrificial elements like manganese had benefits due to preventing chromium depletion. This approach and theoretical thermodynamic analysis are suggested for further studies to fully describe and understand the corrosion mechanism under molten salts at high temperatures. Comparing the corrosion rate, some promising alloys, such as CoCrFeNiTi<sub>0.5</sub> and Al<sub>5</sub>Co<sub>18</sub>Cr<sub>7</sub>Fe<sub>9</sub>Ni<sub>5</sub>1Ti<sub>5</sub>, exhibit 1.4 and 2.0 mg·cm<sup>-2</sup> values, respectively. HEAs have potential applicability in molten salt storage as structural materials for tanks and pipes and as phase change materials for thermal energy storage due to their high melting points, excellent high-temperature strength, good corrosion resistance, and the ability to tailor their composition to specific applications. These unique properties can reduce maintenance and replacement costs and improve energy storage efficiency. However, more research is needed to optimize their properties and identify suitable compositions and processing methods for specific applications. Additionally, HEAs' long-term durability and reliability in high-temperature and corrosive environments must be evaluated before their suitability for industrial-scale applications.

**Acknowledgments:** The authors express their gratitude to the Universidad Mayor.

Funding information: The authors would like to acknowledge the financial support provided through the project following projects: F. Pineda gratefully acknowledges the financial support given by ANID within the project Fondecyt 11200388. C. Martínez acknowledges to ANID the financial support given by Fondecyt Iniciación 11190500. P. Martin gratefully acknowledges ANID/Doctorado Becas Chile/2019-72200338. Finally, C. Aguilar acknowledges to ANID the financial support given by Fondecyt Regular 1230620. Also C. Martínez and C. Aguilar acknowledgement to the Millennium Institute on Green Ammonia as Energy Vector – MIGA (ICN2021\_023).

**Author contributions:** All authors have accepted responsibility for the entire content of this manuscript and approved its submission.

DE GRUYTER High-entropy alloys — 11

**Conflict of interest:** The authors state no conflict of interest.

## References

- [1] He, R. F., M. R. Zhong, and J. B. Huang. The dynamic effects of renewable-energy and fossil-fuel technological progress on metal consumption in the electric power industry. *Resources Policy*, Vol. 71, 2021, id. 101985.
- [2] Adger, N. and A. Fischlin, IPCC, 2014: Summary for Policymakers, Clim. Chanq. 2014 Mitig. Clim. Chanq. 2014. pp. 1–30.
- [3] Al Garni, H., A. Kassem, A. Awasthi, D. Komljenovic, and K. Al-Haddad. A multicriteria decision making approach for evaluating renewable power generation sources in Saudi Arabia. Sustainable Energy Technologies and Assessments, Vol. 16, 2016, pp. 137–150.
- [4] Møller, K. T., T. R. Jensen, E. Akiba, and H. W. Li. Hydrogen A sustainable energy carrier. *Progress in Natural Science: Materials International*, Vol. 27, 2017, pp. 34–40.
- [5] Sahlberg, M., D. Karlsson, C. Zlotea, and U. Jansson. Superior hydrogen storage in high entropy alloys. *Scientific Reports*, Vol. 6, 2016, pp. 1–6.
- [6] Gorsse, S., J. P. Couzinié, and D. B. Miracle. From high-entropy alloys to complex concentrated alloys. *Comptes Rendus Physique*, Vol. 19, 2018, pp. 721–736.
- [7] Praveen, S. and H. S. Kim. High-Entropy Alloys: Potential Candidates for High-Temperature Applications – An Overview. Advanced Engineering Materials, Vol. 20, 2018, pp. 1–22.
- [8] Soto, A. O., A. S. Salgado, and E. B. Niño. Thermodynamic analysis of high entropy alloys and their mechanical behavior in high and low-temperature conditions with a microstructural approach – A review. *Intermetallics*, Vol. 124, 2020, id. 106850.
- [9] Senkov, O. N., D. B. Miracle, K. J. Chaput, and J. P. Couzinie. Development and exploration of refractory high entropy alloys - A review. *Journal of Materials Research*, Vol. 33, 2018, pp. 3092–3128.
- [10] Baykara, S. Z. Hydrogen: A brief overview on its sources, production and environmental impact. *International Journal of Hydrogen Energy*, Vol. 43, 2018, pp. 10605–10614.
- [11] Tarasov, B. P., P. V. Fursikov, A. A. Volodin, M. S. Bocharnikov, Y. Y. Shimkus, A. M. Kashin, et al. Metal hydride hydrogen storage and compression systems for energy storage technologies. *International Journal of Hydrogen Energy*, Vol. 46, 2020, pp. 13647–13657.
- [12] Takagi, S. and S. I. Orimo. Recent progress in hydrogen-rich materials from the perspective of bonding flexibility of hydrogen. *Scripta Materialia*, Vol. 109, 2015, pp. 1–5.
- [13] Aguey-Zinsou, K. F. and J. R. Ares-Fernández. Hydrogen in magnesium: New perspectives toward functional stores. *Energy & Environmental Science*, Vol. 3, 2010, pp. 526–543.
- [14] Luo, Q., J. Li, B. Li, B. Liu, H. Shao, and Q. Li. Kinetics in Mg-based hydrogen storage materials: Enhancement and mechanism. *Journal of Magnesium and Alloys*, Vol. 7, 2019, pp. 58–71.
- [15] Pang, Y. and Q. Li. A review on kinetic models and corresponding analysis methods for hydrogen storage materials. *International Journal of Hydrogen Energy*, Vol. 41, 2016, pp. 18072–18087.
- [16] Rusman, N. A. A. and M. Dahari. A review on the current progress of metal hydrides material for solid-state hydrogen storage applications. *International Journal of Hydrogen Energy*, Vol. 41, 2016, pp. 12108–12126.

[17] Zhang, X. L., Y. F. Liu, X. Zhang, J. J. Hu, M. X. Gao, and H. G. Pan. Empowering hydrogen storage performance of MgH2 by nanoengineering and nanocatalysis. *Materials Today Nano*, Vol. 9, 2020, id. 100064.

- [18] Zaluska, A., L. Zaluski, and J. O. Ström-Olsen. Nanocrystalline magnesium for hydrogen storage. *Journal of Alloys and Compounds*, Vol. 288, 1999, pp. 217–225.
- [19] Bellosta von Colbe, J., J. R. Ares, J. Barale, M. Baricco, C. Buckley, G. Capurso, et al. Application of hydrides in hydrogen storage and compression: Achievements, outlook and perspectives. *International Journal of Hydrogen Energy*, Vol. 44, 2019, pp. 7780–7808.
- [20] El Kharbachi, A., E. M. Dematteis, K. Shinzato, S. C. Stevenson, L. J. Bannenberg, M. Heere, et al. Energy carriers for novel hydrogen and electrochemical storage. *The Journal of Physical Chemistry C*, Vol. 124, 2020, pp. 7599–7607.
- [21] Barlev, D., R. Vidu, and P. Stroeve. Innovation in concentrated solar power. *Solar Energy Materials & Solar Cells*, Vol. 95, 2011, pp. 2703–2725.
- [22] Walczak, M., F. Pineda, Á.G. Fernández, C. Mata-Torres, and R. A. Escobar. Materials corrosion for thermal energy storage systems in concentrated solar power plants. *Renewable and Sustainable Energy*, Vol. 86, 2018, pp. 22–44.
- [23] Vignarooban, K., X. Xu, A. Arvay, K. Hsu, and A. M. Kannan. Heat transfer fluids for concentrating solar power systems – A review. *Applied Energy*, Vol. 146, 2015, pp. 383–396.
- [24] Grosu, Y., O. Bondarchuk, and A. Faik. The effect of humidity, impurities and initial state on the corrosion of carbon and stainless steels in molten HitecXL salt for CSP application. Solar Energy Materials & Solar Cells, Vol. 174, 2018, pp. 34–41.
- [25] Islam, M. T., N. Huda, A. B. Abdullah, and R. Saidur. A comprehensive review of state-of-the-art concentrating solar power (CSP) technologies: Current status and research trends. *Renewable and Sustainable Energy*, Vol. 91, 2018, pp. 987–1018.
- [26] Vignarooban, K., X. Xu, K. Wang, E. E. Molina, P. Li, D. Gervasio, et al. Vapor pressure and corrosivity of ternary metal-chloride molten-salt based heat transfer fluids for use in concentrating solar power systems. *Applied Energy*, Vol. 159, 2015, pp. 206–213.
- [27] Peng, Q., X. Yang, J. Ding, X. Wei, and J. Yang. Design of new molten salt thermal energy storage material for solar thermal power plant. *Applied Energy*, Vol. 112, 2013, pp. 682–689.
- [28] Myers, P. D. and D. Y. Goswami. Thermal energy storage using chloride salts and their eutectics. *Applied Thermal Engineering*, Vol. 109, 2016, pp. 889–900.
- [29] Moreno, P., L. Miró, A. Solé, C. Barreneche, C. Solé, I. Martorell, et al. Corrosion of metal and metal alloy containers in contact with phase change materials (PCM) for potential heating and cooling applications. *Applied Energy*, Vol. 125, 2014, pp. 238–245.
- [30] Sastri, V. S., E. Ghali, and M. Elboujdaini. Corrosion Prevention and Protection: Practical Solutions, John Wiley & Sons, The Atrium, Southern Gate, Chichester, West Sussex England, 2012.
- [31] Xu, X., K. Vignarooban, B. Xu, K. Hsu, and A. M. Kannan. Prospects and problems of concentrating solar power technologies for power generation in the desert regions. *Renewable and Sustainable Energy*, Vol. 53, 2016, pp. 1106–1131.
- [32] Papaelias, M., L. Cheng, M. Kogia, A. Mohimi, V. Kappatos, C. Selcuk, et al. Inspection and Structural Health Monitoring techniques for Concentrated Solar Power plants. *Renewable Energy*, Vol. 85, 2016, pp. 1178–1191.

- [33] Fernández, A. G. G., H. Galleguillos, E. Fuentealba, and F. J. J. Pérez. Corrosion of stainless steels and low-Cr steel in molten Ca (NO3)2–NaNO3–KNO3 eutectic salt for direct energy storage in CSP plants. *Solar Energy Materials & Solar Cells*, Vol. 141, 2015, pp. 7–13.
- [34] Mohammadi Zahrani, E. and A. M. Alfantazi. Molten salt induced corrosion of Inconel 625 superalloy in PbSO4-Pb3O4-PbCl2-Fe2O3-ZnO environment. *Corrosion Science*, Vol. 65, 2012, pp. 340-359.
- [35] Fernández, A. G., A. Rey, I. Lasanta, S. Mato, M. P. Brady, and F. J. Perez. Corrosion of alumina-forming austenitic steel in molten nitrate salts by gravimetric analysis and impedance spectroscopy. *Materials and Corrosion*, Vol. 65, 2014, pp. 267–275.
- [36] Pérez, F. J., M. P. Hierro, and J. Nieto. Waste incineration corrosion processes: Oxidation mechanisms by electrochemical impedance spectroscopy. *Materials and Corrosions*, Vol. 59, 2008, pp. 566–572.
- [37] Ni, C. S. S., L. Y. Y. Lu, C. L. L. Zeng, and Y. Niu. Evaluation of corrosion resistance of aluminium coating with and without annealing against molten carbonate using electrochemical impedance spectroscopy. *Journal of Power Sources*, Vol. 261, 2014, pp. 162–169.
- [38] Diaz, E. F., C. Cuevas-Arteaga, N. Flores-García, S. Mejía Sintillo, and O. Sotelo-Mazón. Corrosion performance of AISI-309 exposed to molten salts V2O5-Na2SO4 at 700°C applying EIS and Rp electrochemical techniques. *Journal of Spectroscopy*, 2015, pp. 1–12.
- [39] Mahobia, G. S., N. Paulose, S. L. Mannan, R. G. Sudhakar, K. Chattopadhyay, N. C. Santhi Srinivas, et al. Effect of hot corrosion on low cycle fatigue behavior of superalloy IN718. *International Journal of Fatigue*, Vol. 59, 2014, pp. 272–281.
- [40] Dutta, S., K. Coscia, and S. Mohapatra. Understanding Corrosion and its Inhibition in Chloride Based Molten Salt Heat- Transfer Fluids used in Concentrated Solar Power Plants. NACE Corros. 2013 Int. Conf. Expo – Pap, Vol. 2669, 2013, pp. 1–10.
- [41] Kruizenga, A. and D. Gill. Corrosion of iron stainless steels in molten nitrate salt. *Energy Procedia*, Vol. 49, 2013, pp. 878–887.
- [42] Fernández, A. G., M. Cortes, E. Fuentealba, and F. J. Pérez. Corrosion properties of a ternary nitrate/nitrite molten salt in concentrated solar technology. *Renewable Energy*, Vol. 80, 2015, pp. 177–183.
- [43] Kruizenga, A. M., D. D. Gill, M. Laford, and G. Mcconohy. Corrosion of High Temperature Alloys in Solar Salt at 400, 500, and 680°C. Sandia National Laboratories, Albuquerque, New Mexico, Sandia report 8256, 2013, pp. 1–45.
- [44] Bradshaw, R. W. and W. M. Clift. Effect of chloride content of molten nitrate salt on corrosion of A516 carbon steel. Sandia National Laboratories, Albuquerque, New Mexico, Sandia Report 7594, 2013, pp. 1–27.
- [45] McConohy, G. and A. Kruizenga. Molten nitrate salts at 600 and 680°C: Thermophysical property changes and corrosion of high-temperature nickel alloys. *Solar Energy*, Vol. 103, 2014, pp. 242–252.
- [46] Ni, C. S., L. Y. Lu, C. L. Zeng, and Y. Niu. Electrochemical impedance studies of the initial-stage corrosion of 310S stainless steel beneath thin film of molten (0.62Li,0.38K)2CO3 at 650°C. Corrosion Science, Vol. 53, 2011, pp. 1018–1024.
- [47] Guo, L., Y. Yue, T. J. Pan, Z. F. Tang, and W. Liu. Corrosion behavior of Ni-Al alloys beneath chlorides melt salt at 700°C. Solar Energy, Vol. 184, 2019, pp. 657–663.
- [48] Shi, H., C. Tang, A. Jianu, R. Fetzer, A. Weisenburger, M. Steinbrueck, et al. Oxidation behavior and microstructure

- evolution of alumina-forming austenitic & high entropy alloys in steam environment at 1200°C. *Corrosion Science*, Vol. 170, 2020, id. 108654.
- [49] Jedlinski, J. The oxidation behaviour of FeCrAl "alumina forming" alloys at high temperatures. *Solid State Ionics*, Vol. 101–103, 1997, pp. 1033–1040.
- [50] Gomez-Vidal, J. C., A. G. Fernández, R. Tirawat, C. Turchi, and W. Huddleston. Corrosion resistance of alumina-forming alloys against molten chlorides for energy production. I: Pre-oxidation treatment and isothermal corrosion tests. *Solar Energy Materials & Solar Cells*, Vol. 166, 2017, pp. 222–233.
- [51] Klenk, A., M. Speicher, and K. Maile. Weld behavior of martensitic steels and ni-based alloys for high temperature components. *Procedia Engineering*, Vol. 55, 2013, pp. 414–420.
- [52] Shi, Y., B. Yang, and P. K. Liaw. Corrosion-resistant high-entropy alloys: A review. *Metals (Basel)*, Vol. 7, 2017, pp. 1–18.
- [53] Ayyagari, A., V. Hasannaeimi, H. S. Grewal, H. Arora, and S. Mukherjee. Corrosion, erosion and wear behavior of complex concentrated alloys: A review. *Metals*, Vol. 8, 2018, id. 603.
- [54] Cantor, B., I. T. H. Chang, P. Knight, and A. J. B. Vincent. Microstructural development in equiatomic multicomponent alloys. *Materials Science & Engineering, A: Structural Materials:* Properties, Microstructure and Processing, Vol. 375–377, 2004, pp. 213–218.
- [55] Yeh, J. W., S. K. Chen, S. J. Lin, J. Y. Gan, T. S. Chin, T. T. Shun, et al. Nanostructured high-entropy alloys with multiple principal elements: Novel alloy design concepts and outcomes. *Advanced Engineering Materials*, Vol. 6, 2004, pp. 299–303.
- [56] Steurer, W. Single-phase high-entropy alloys A critical update. Materials Characterization, Vol. 162, 2020, id. 110179.
- [57] Miracle, D. B. and O. N. Senkov. A critical review of high entropy alloys and related concepts. *Acta Materialia*, Vol. 122, 2017, pp. 448–511.
- [58] Cantor, B. Multicomponent high-entropy Cantor alloys. Progress in Materials Science, Vol. 20, 2020, id. 100754.
- [59] Senkov, O. N., G. B. Wilks, D. B. Miracle, C. P. Chuang, and P. K. Liaw. Refractory high-entropy alloys. *Intermetallics*, Vol. 18, 2010, pp. 1758–1765.
- [60] Senkov, O. N., G. B. Wilks, J. M. Scott, and D. B. Miracle. Mechanical properties of Nb25Mo25Ta25W25 and V20Nb20Mo 20Ta20W20 refractory high entropy alloys. *Intermetallics*, Vol. 19, 2011, pp. 698–706.
- [61] Youssef, K. M., A. J. Zaddach, C. Niu, D. L. Irving, C. C. Koch, K. M. Youssef, et al. A novel low-density, high-hardness, high- entropy alloy with close-packed single-phase nanocrystalline structures. *Materials Research Letters*, Vol. 3831, 2015, pp. 95–99.
- [62] Takeuchi, A., K. Amiya, T. Wada, and K. Yubuta. Dual HCP structures formed in senary ScYLaTiZrHf multi-principal-element alloy. *Intermetallics*, Vol. 69, 2016, pp. 103–109.
- [63] Hammond, V. H., M. A. Atwater, K. A. Darling, and H. Q. Nguyen. Equal-channel angular extrusion of a low-density high-entropy alloy produced by high-energy cryogenic mechanical alloying. *JOM*, Vol. 66, 2021, pp. 2021–2029.
- [64] Yurchenko, N., N. Stepanov, and G. Salishchev. Laves-phase formation criterion for high-entropy alloys. *Materials Science and Technology*. (United Kingdom), Vol. 33, 2017, pp. 17–22.
- [65] Kube, S. A., S. Sohn, D. Uhl, A. Datye, A. Mehta, and J. Schroers. Phase selection motifs in High Entropy Alloys revealed through combinatorial methods: Large atomic size difference favors BCC over FCC. Acta Materialia, Vol. 166, 2019, pp. 677–686.

High-entropy alloys — 13

- [66] Kao, Y. F., S. K. Chen, J. H. Sheu, J. T. Lin, W. E. Lin, J. W. Yeh, et al. Hydrogen storage properties of multi-principal-component CoFeMnTixVyZrz alloys. *International Journal of Hydrogen Energy*, Vol. 35, 2010, pp. 9046–9059.
- [67] Bielmann, M., S. Kato, P. Mauron, A. Borgschulte, and A. Züttel. Characterization of hydrogen storage materials by means of pressure concentration isotherms based on the mass flow method. *Review of Scientific Instruments*, Vol. 80, 2009, id. 083901.
- [68] Chen, S. K., P. H. Lee, H. Lee, and H. T. Su. Hydrogen storage of C14-CruFevMnwTixVyZrz alloys. *Materials Chemistry and Physics*, Vol. 210, 2018, pp. 336–347.
- [69] Zadorozhnyy, V., B. Sarac, E. Berdonosova, T. Karazehir, A. Lassnig, C. Gammer, et al. Evaluation of hydrogen storage performance of ZrTiVNiCrFe in electrochemical and gas-solid reactions. *International Journal of Hydrogen Energy*, Vol. 45, 2020, pp. 5347–5355.
- [70] Sarac, B., V. Zadorozhnyy, E. Berdonosova, Y. P. Ivanov, S. Klyamkin, S. Gumrukcu, et al. Hydrogen storage performance of the multi-principal-component CoFeMnTiVZr alloy in electrochemical and gas-solid reactions. RSC Advances, Vol. 10, 2020, pp. 24613–24623.
- [71] Edalati, P., R. Floriano, A. Mohammadi, Y. Li, G. Zepon, H. W. Li, et al. Reversible room temperature hydrogen storage in high-entropy alloy TiZrCrMnFeNi. *Scripta Materialia*, Vol. 178, 2020, pp. 387–390.
- [72] Marques, F., H. C. Pinto, S. J. A. Figueroa, F. Winkelmann, M. Felderhoff, W. J. Botta, et al. Mg-containing multi-principal element alloys for hydrogen storage: A study of the MgTiNbCr0.5Mn0.5Ni0.5 and Mg0.68TiNbNi0.55 compositions. *International Journal of Hydrogen Energy*, Vol. 5, 2020, pp. 19539–19552.
- [73] Zhang, J., D. W. Zhou, L. P. He, P. Peng, and J. S. Liu. First-principles investigation of Mg2Ni phase and high/low temperature Mg2NiH4 complex hydrides. *Journal of Physics and Chemistry of Solids*, Vol. 70, 2009, pp. 32–39.
- [74] Hu, J., H. Shen, M. Jiang, H. Gong, H. Xiao, Z. Liu, et al. A DFT study of hydrogen storage in high-entropy alloy TiZrHfScMo. *Nanomaterials*, Vol. 9, 2019, pp. 1–12.
- [75] Shen, H., J. Zhang, J. Hu, J. Zhang, Y. Mao, H. Xiao, et al. A novel TiZrHfMoNb high-entropy alloy for solar thermal energy storage. *Nanomaterials*, Vol. 9, 2019, pp. 1–9.
- [76] Shen, H., J. Hu, P. Li, G. Huang, J. Zhang, J. Zhang, et al. Compositional dependence of hydrogenation performance of Ti-Zr-Hf-Mo-Nb high-entropy alloys for hydrogen/tritium storage. *Journal of Materials Science & Technology*, Vol. 55, 2020, pp. 116–125.
- [77] Montero, J., C. Zlotea, G. Ek, J. Crivello, L. Laversenne, and M. Sahlberg. TiVZrNb multi-principal-element alloy: Synthesis optimization, structural, and hydrogen sorption properties. *Molecules*, Vol. 24, 2019, pp. 2799–2813.
- [78] Montero, J., G. Ek, L. Laversenne, V. Nassif, G. Zepon, M. Sahlberg, et al. Hydrogen storage properties of the refractory Ti-V-Zr-Nb-Ta multi-principal element alloy. *Journal of Alloys and Compounds*, Vol. 835, 2020, id. 155376.
- [79] Zepon, G., D. R. Leiva, R. B. Strozi, A. Bedoch, S. J. A. Figueroa, T. T. Ishikawa, et al. Hydrogen-induced phase transition of MgZrTiFe0.5Co0.5Ni0.5 high entropy alloy. *International Journal of Hydrogen Energy*, Vol. 43, 2018, pp. 1702–1708.

- [80] Zlotea, C., M. A. Sow, G. Ek, J. P. Couzinié, L. Perrière, I. Guillot, et al. Hydrogen sorption in TiZrNbHfTa high entropy alloy. *Journal of Alloys and Compounds*, Vol. 775, 2019, pp. 667–674.
- [81] Karlsson, D., G. Ek, J. Cedervall, C. Zlotea, K. T. Møller, T. C. Hansen, et al. Structure and Hydrogenation Properties of a HfNbTiVZr High-Entropy Alloy. *Inorganic Chemistry*, Vol. 57, 2018, pp. 2103–2110.
- [82] Nygård, M. M., G. Ek, D. Karlsson, M. Sahlberg, M. H. Sørby, and B. C. Hauback. Hydrogen storage in high-entropy alloys with varying degree of local lattice strain. *International Journal of Hydrogen Energy*, Vol. 44, 2019, pp. 29140–29149.
- [83] Dewangan, S. K., V. K. Sharma, P. Sahu, and V. Kumar. Synthesis and characterization of hydrogenated novel AlCrFeMnNiW high entropy alloy. *International Journal of Hydrogen Energy*, Vol. 45, 2019, pp. 16984–16991.
- [84] Kunce, I., M. Polanski, and J. Bystrzycki. Structure and hydrogen storage properties of a high entropy ZrTiVCrFeNi alloy synthesized using Laser Engineered Net Shaping (LENS). *International Journal of Hydrogen Energy*, Vol. 38, 2013, pp. 12180–12189.
- [85] de Marco, M. O., Y. Li, H. W. Li, K. Edalati, and R. Floriano. Mechanical Synthesis and Hydrogen Storage Characterization of MgVCr and MgVTiCrFe High-Entropy Alloy. *Advanced Engineering Materials*, Vol. 22, 2020, pp. 1–9.
- [86] Marques, S. C., A. V. Castilho, and D. S. dos Santos. Effect of alloying elements on the hydrogen diffusion and trapping in high entropy alloys. *Scripta Materialia*, Vol. 201, 2021, id. 113957.
- [87] Chen, H., Y. Ma, C. Li, Q. Zhao, Y. Huang, H. Luo, et al. A nano-sized NbC precipitation strengthened FeCoCrNi high entropy alloy with superior hydrogen embrittlement resistance. *Corrosion Science*, Vol. 208, 2022, id. 110636.
- [88] Sotelo-Mazón, O., C. Cuevas-Arteaga, J. Porcayo-Calderón, V. M. Salinas Bravo, and G. Izquierdo-Montalvo. Corrosion behavior of pure Cr, Ni, and Fe exposed to molten salts at high temperature. Advances in Materials Science and Engineering, Vol. 2014, 2014, pp. 1–12.
- [89] Jalbuena, A. A., N. Ury, J. Bae, C. Faraj, K. Hanan, S. Kasnakjian, et al. Corrosion of Al0.1CoCrFeNi high entropy alloy in a molten eutectic salt. *Journal of the Electrochemical Society*. Vol. 166, 2019, pp. C3488–C3492.
- [90] Tsao, T. K., A. C. Yeh, C. M. Kuo, and H. Murakami. High temperature oxidation and corrosion properties of high entropy superalloys. *Entropy*, Vol. 18, 2016, pp. 1–13.
- [91] Daoud, H. M., A. M. Manzoni, R. Völkl, N. Wanderka, and U. Glatzel. Oxidation Behavior of Al8Co17Cr17Cu8Fe17Ni33, Al23Co15Cr23Cu8Fe15Ni15, and Al17Co17Cr17Cu17Fe17Ni17 compositionally complex alloys (high-entropy alloys) at elevated temperatures in air. Advanced Engineering Materials, Vol. 17, 2015, pp. 1134–1141.
- [92] Li, C., J. C. Li, M. Zhao, and Q. Jiang. Effect of aluminum contents on microstructure and properties of AlxCoCrFeNi alloys. *Journal of Alloys and Compounds*, Vol. 504, 2010, pp. 515–518.
- [93] Wang, W. R., W. L. Wang, S. C. Wang, Y. C. Tsai, C. H. Lai, and J. W. Yeh. Effects of Al addition on the microstructure and mechanical property of AlxCoCrFeNi high-entropy alloys. *Intermetallics*, Vol. 26, 2012, pp. 44–51.
- [94] Wang, W. R., W. L. Wang, and J. W. Yeh. Phases, microstructure and mechanical properties of AlxCoCrFeNi high-entropy alloys at elevated temperatures. *Journal of Alloys and Compounds*, Vol. 589, 2014, pp. 143–152.

- [95] Kao, Y. F., T. J. Chen, S. K. Chen, and J. W. Yeh. Microstructure and mechanical property of as-cast, -homogenized, and -deformed AlxCoCrFeNi ( $0 \le x \le 2$ ) high-entropy alloys. *Journal of Alloys and Compounds*, Vol. 488, 2009, pp. 57–64.
- [96] Raghavan, R., K. C. Hari Kumar, and B. S. Murty. Analysis of phase formation in multi-component alloys. *Journal of Alloys and Compounds*, Vol. 544, 2012, pp. 152–158.
- [97] Liu, W. H., Y. Wu, J. Y. He, Y. Zhang, C. T. Liu, and Z. P. Lu. The Phase Competition and Stability of High-Entropy Alloys. *JOM*, Vol. 66, 2014, pp. 1973–1983.
- [98] Moon, J. T., E. J. Schindelholz, M. A. Melia, A. B. Kustas, and D. Chidambaram. Corrosion of Additively Manufactured CoCrFeMnNi High Entropy Alloy in Molten NaNO3-KNO3. *Journal of the Electrochemical Society*, Vol. 167, 2020, id. 081509.
- [99] Xie, Y., H. Cheng, Q. Tang, W. Chen, W. Chen, and P. Dai. Effects of N addition on microstructure and mechanical properties of CoCrFeNiMn high entropy alloy produced by mechanical alloying and vacuum hot pressing sintering. *Intermetallics*, Vol. 93, 2018, pp. 228–234.
- [100] Ji, W., W. Wang, H. Wang, J. Zhang, Y. Wang, F. Zhang, et al. Alloying behavior and novel properties of CoCrFeNiMn highentropy alloy fabricated by mechanical alloying and spark plasma sintering. *Intermetallics*, Vol. 56, 2015, pp. 24–27.
- [101] Wu, Z., H. Bei, F. Otto, G. M. Pharr, and E. P. George. Recovery, recrystallization, grain growth and phase stability of a family of FCC-structured multi-component equiatomic solid solution alloys. *Intermetallics*, Vol. 46, 2014, pp. 131–140.
- [102] Elbakhshwan, M., W. Doniger, C. Falconer, M. Moorehead, C. Parkin, C. Zhang, et al. Corrosion and Thermal Stability of CrMnFeNi High Entropy Alloy in Molten FLiBe Salt. Scientific Reports, Vol. 9, 2019, pp. 1–10.
- [103] Zhao, Y., N. Klammer, and J. Vidal. Purification strategy and effect of impurities on corrosivity of dehydrated carnallite for thermal solar applications. *RSC Advances*, Vol. 9, 2019, pp. 41664–41671.
- [104] Ping, L., Z. Jie, L. Tingju, and P. Shengjiao. Hot corrosion behaviors of CoCrFeNiTi0.5 high entropy alloy in the mixture salt of Na2SO4-25%K2SO4 and Na2SO4-25%NaCl at 750°C. Advanced Materials, Vol. 8, 2019, id. 120.
- [105] Musabikha, S. and I. Ketut Aria Pria Utama. Corrosion in the marine renewable energy: a review. *International Journal of Environmental Research Clean Energy*, Vol. 7, 2017, pp. 1–9.
- [106] Momber, A. Corrosion and corrosion protection of support structures for offshore wind energy devices (OWEA). *Mater. Corros*, Vol. 62, 2011, pp. 391–404.

- [107] Traverso, P. and E. Canepa. A review of studies on corrosion of metals and alloys in deep-sea environment. *Ocean Engineering*, Vol. 87, 2014, pp. 10–15.
- [108] Soltani, M., F. Moradi, M. Souri, and B. Rafiei. Environmental, economic, and social impacts of geothermal energy systems. *Renewable and Sustainable Energy*, Vol. 140, 2021, id. 110750.
- [109] Butler, T. M. and K. J. Chaput. Native oxidation resistance of Al20Nb30Ta10Ti30Zr10 refractory complex concentrated alloy (RCCA). *Journal of Alloys and Compounds*, Vol. 787, 2019, pp. 606–617.
- [110] Karlsdottir, S. N., I. Csaki, I. V. Antoniac, C. A. Manea, R. Stefanoiu, F. Magnus, et al. Corrosion behavior of AlCrFeNiMn high entropy alloy in a geothermal environment. *Geothermics*, Vol. 81, 2019, pp. 32–38.
- [111] Wang, S., Z. Chen, P. Zhang, K. Zhang, C. L. Chen, and B. L. Shen. Influence of Al content on high temperature oxidation behavior of AlxCoCrFeNiTi0.5 high entropy alloys. *Vacuum*, Vol. 163, 2019, pp. 263–268.
- [112] Mohanty, A., J. K. Sampreeth, O. Bembalge, J. Y. Hascoet, S. Marya, R. J. Immanuel, et al. High temperature oxidation study of direct laser deposited AlXCoCrFeNi (X = 0.3,0.7) high entropy alloys. Surface and Coatings Technology, Vol. 380, 2019, id. 125028.
- [113] Kai, W., C. C. Li, F. P. Cheng, K. P. Chu, R. T. Huang, L. W. Tsay, et al. The oxidation behavior of an equimolar FeCoNiCrMn highentropy alloy at 950°C in various oxygen-containing atmospheres. *Corrosion Science*, Vol. 108, 2016, pp. 209–214.
- [114] Miracle, D. B., J. D. Miller, O. N. Senkov, C. Woodward, M. D. Uchic, and J. Tiley. Exploration and development of high entropy alloys for structural applications. *Entropy*, Vol. 16, 2014, pp. 494–525.
- [115] Ma, Y., Y. Ma, Q. Wang, S. Schweidler, M. Botros, T. Fu, et al. Highentropy energy materials\_ challenges and new opportunities. *Energy & Environmental Science*, Vol. 14, 2021, pp. 2883–2905.
- [116] Kunce, I., M. Polanski, and J. Bystrzycki. Microstructure and hydrogen storage properties of a TiZrNbMoV high entropy alloy synthesized using Laser Engineered Net Shaping (LENS). *International Journal of Hydrogen Energy*, Vol. 39, 2014, pp. 9904–9910.
- [117] Zhang, C., A. Song, Y. Yuan, Y. Wu, P. Zhang, Z. Lu, et al. Study on the hydrogen storage properties of a TiZrNbTa high entropy alloy. *International Journal of Hydrogen Energy*, Vol. 45, 2020, pp. 5367–5374.
- [118] Zhang, C., Y. Wu, L. You, X. Cao, Z. Lu, and X. Song. Investigation on the activation mechanism of hydrogen absorption in TiZrNbTa high entropy alloy. *Journal of Alloys and Compounds*, Vol. 781, 2019, pp. 613–620.